iScience

CellPress
OPEN ACCESS

Article

Structural health monitoring of sabo check dams with cosmic-ray muography

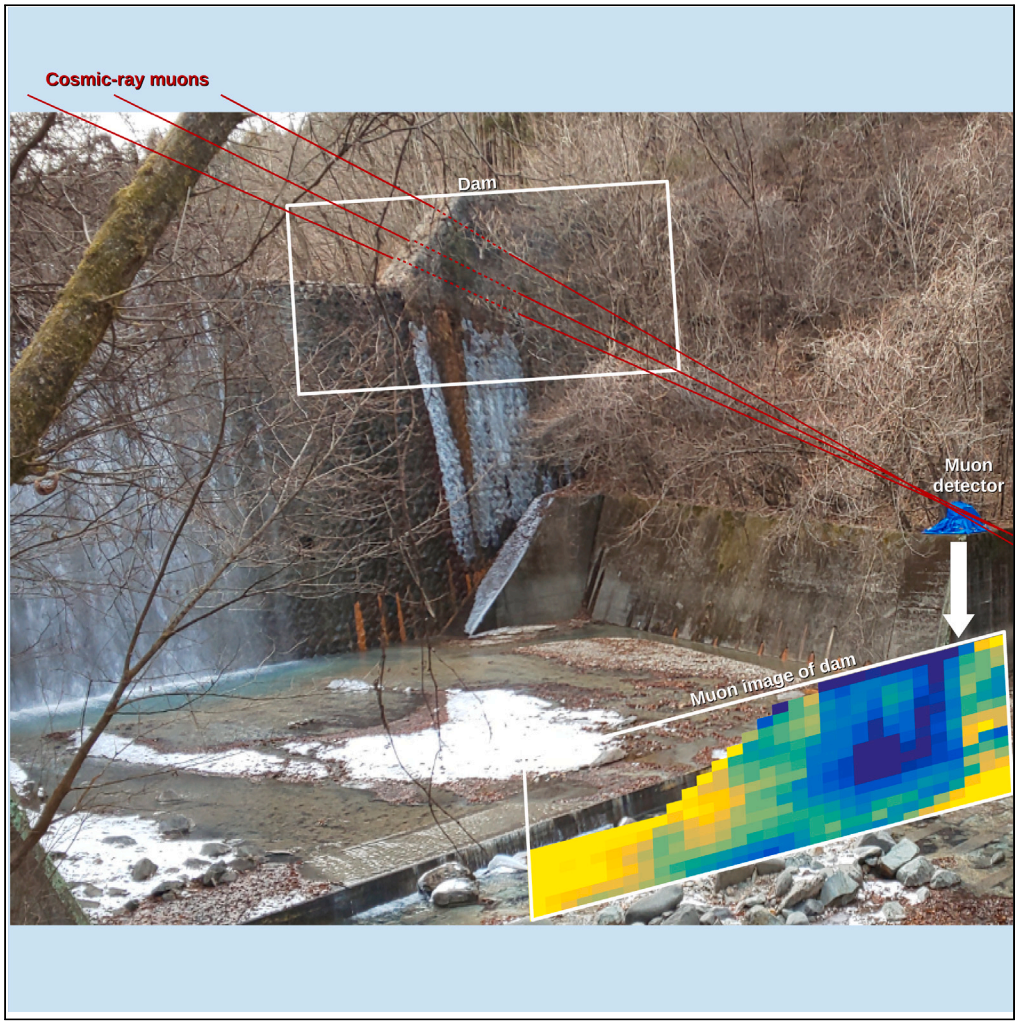

László Oláh, Hiroyuki K.M. Tanaka, Toshio Mori, Yukihiko Sakatani, Dezső Varga

olah.laszlo@wigner.hu

Highlights

Cosmic muons were used for imaging a sabo check dam for the first time

Muographic density image of the dam revealed an internal deterioration

Muography offers passive, remote, and non-destructive inspection of dam structures

Oláh et al., iScience *26*, 108019
October 20, 2023
https://doi.org/10.1016/j.isci.2023.108019

iScience

CellPress
OPEN ACCESS

Article

Structural health monitoring of sabo check dams with cosmic-ray muography

László Oláh,[1,2,3,6,*] Hiroyuki K.M. Tanaka,[1,2,3] Toshio Mori,[4] Yukihiko Sakatani,[4] and Dezső Varga[3,5]

SUMMARY

Debris dams have a crucial role in consolidation of river basins and allow erosion control, flood protection in mountainous areas. Many of these infrastructures have operated over five decades, thus structural health monitoring (SHM) of these infrastructures became timely due to their aging. Utilizing new techniques is required for inspecting a large number of dams and deciding about their reinforcement or reconstruction. In this work, we propose cosmic-ray muography as a complementary tool for the SHM of debris dams. We conducted the first muographic surveying of a sabo check dam in the Karasu River, Gunma, Japan. The average mass density image was produced with a spatial resolution of 0.5 m through the dam. The comparison of density data reconstructed by muography and gamma-ray logging suggest the internal deterioration of dam in the region where cement released out from the embankment body.

INTRODUCTION

Debris flows are fast-moving mixtures of water, soil, and rock that occur when intense rain falls, snow melts, volcanic activities trigger landslides and debris-covered mountain slopes erode.[1] The relatively high mass density (>1.5 gcm^{-3}) and velocity (>10 ms^{-1}) allows this phenomenon to entrain the materials from the river bed and bank and grow its size and hazardous potential. Dynamics of erosion and deposition of transported materials are mainly controlled by the flow parameters,[1] the slope and wetness of bed[2] and the memory effects.[3] Debris flows can drastically change the geomorphology in mountainous regions and run out for long distances within a few tens of kilometers. Debris flows pose catastrophic threat to landscapes, societies and economies.[4] For example, torrential rains triggered debris flows and mud flows that destroyed local infrastructures and killed ten thousands of people in Vargas State, Venezuela, in 1999.[5] The number of the occurrence of sediment catastrophes are expected to increase in the next decades due to the change of climate[6] that motivates the improvement of mitigating techniques. Two types of measures are applied to reduce the impact of debris flows[7]: Passive measures aim to minimize the damages caused by debris flows. This includes creating evacuation systems, hazard mapping,[8] installing monitoring and warning systems (e.g., ref. [9,10]), flow modeling and run-out prediction,[11] etc. Active measures aim to control the spatiotemporal evolution of debris flows from triggering to deposition by constructing infrastructures, such as dams or channels, for energy dissipation and erosion control (e.g., ref. [12–14]). Check dams, also called sabo (sa-bo means 'sand protection') dams, are constructed for consolidation and stabilization of river basins, decrease of bed slopes, retention of sediments, regulation of solid discharges at different mountainous regions worldwide (e.g., ref. [15,16]). Series of dams are applied along rivers and the number of dams reach a few tens of thousands at each mountainous region. The design and structure of check dams depend on the local focus of erosion control, e.g., soil bioengineering dams are made from wood and cobble, civil engineering dams are made from rock and concrete. In Japan, most of the so-called sabo dams are made from concrete and rock to adapt the more intense rainfalls and volcanic activities that can result in intense outburst floods and mudflows (lahars). A few tens of thousands of sabo dams were made from rubble-concrete (debris dams) before the 1970s. The aging and internal deterioration of sabo dams is expected at numerous sites after a period of over half century. The maintenance of sabo dams has become necessary to provide erosion control in the mountainous regions. SHM of these infrastructures are required to decide which ones have to be reinforced or even rebuilt.

The SHM of concrete and rock-filled dams is performed for identifying anomalous behaviors and allowing construction control, design verification, performance evaluation and safety. Various techniques have been utilized for SHM of dams besides traditional visual inspections and a huge arsenal of statistical and deterministic analyses techniques have been developed for evaluating the future behaviors.[17] Here, we provide a brief description of available techniques without claiming completeness. Automated sensors measure water's parameters (e.g., level, flow, pressure, etc.) for monitoring of the reservoir level, the inflow and the precipitation at the upstream side, as well as the outflow at the downstream side. The continuous monitoring of slope stability, dam deformations and internal strains help to recognize the structural responses of dams. Piezometric level sensors are utilized to measure pore-water pressures in real-time for localizing the possible seepages.[18]

[1]Earthquake Research Institute, The University of Tokyo, 1-1-1 Yayoi, Bunkyo, Tokyo 113-0032, Japan
[2]International Muography Research Organization (MUOGRAPHIX), The University of Tokyo, 1-1-1 Yayoi, Bunkyo-ku, Tokyo 113-0032, Japan
[3]International Virtual Muography Institute (VMI), Global, Tokyo, Japan
[4]Sabo Frontier Foundation, Tokyo, Japan
[5]Wigner Research Centre for Physics, Hungarian Research Network, 29-33 Konkoly-Thege Miklós Str., 1121 Budapest, Hungary
[6]Lead contact
*Correspondence: olah.laszlo@wigner.hu
https://doi.org/10.1016/j.isci.2023.108019

Figure 1. The photograph of the inspected sabo dam in the Karasu River, Gunma, Japan

A black rectangle bounds the inspected region of the dam. Two white rectangles highlight the regions which from cement releasing out from the embankment body of the dam. A white arrow shows the orientation of the muographic observation system (MOS).

Extensometers are applied to measure the relative displacements between the base rocks and dam foundations. Fiber optics are applied for measuring the surface deformations on dams.[19] The main limitations of these techniques is that their operation requires boreholes in the dams. Terrestrial laser scanners (TLS),[20] global positioning systems[21] and synthetic aperture radars[22] are utilized precise (at the order of a few millimeters) measurement of surface displacements without boreholes. These techniques have potential to allow real-time deformation monitoring, however samplings are not yet continuous. Besides vertical displacements, the lateral movement of dam foundations can be measured by inclinometers. Thermometers are applied for continuous monitoring of air temperature that is an input for time-series analysis of stress and deformation data.[23] High-resolution seismography[24] and electrical resistivity tomography (ERT)[25] are applied for assessing the internal structure of dams by means of detecting anomalies caused by structural failures (such as fractures or long-term degradation). A main limitation of these techniques is that these are not passive, i.e., these applying signal sources on the surface for imaging the subsurface structure of dams. Furthermore, the accessibility of ERT to the subsurface is limited to a few meters.

Cosmic-ray muons allowing the passive, remote and non-destructive scanning of large-sized natural and human-made objects like as X-raying is utilized for imaging the bones in human bodies.[26,27] The muons are naturally occurring elementary particles which are created in the upper (typically at 10–15 km a.s.l.) atmosphere as decay products of secondary particles originating from the collisions of primary

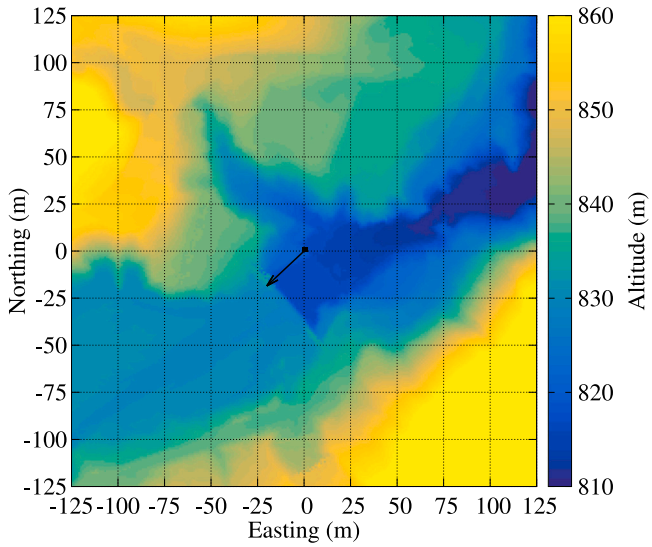

Figure 2. The topographic map of the measurement is shown for an area of 250 m × 250 m around the location of the MOS (0,0)

The origo corresponds to a latitude of 36.437 N°, a longitude of 138.684 E° and an altitude of 819.6 m above sea level. A black arrow shows the horizontal orientation and distance of the MOS from the sabo dam which were set to 227° from north and 26.1 m, respectively. This topographic map is based on the data of Tone River Basin Sabo Office of the Ministry of Land, Infrastructure, Transport and Tour.

Figure 3. A photograph about the installation of muographic observations system at one of the sabo dams of Karasu River

cosmic-rays with atmospheric nuclei. Muons are penetrating down in the atmosphere and are being everywhere on the Earth surface with a typical yield of approx. 10000 per square meter per minute. The muons can penetrate even a few hundred meters of rock with suffering a minimal deflections along their paths. Particle detectors are applied for angular dependent tracking the muons penetrating the targeted objects. Using the measured angular dependent muon count maps, the corresponding projective density distributions are determined through the objects via flux modeling. The number of the applications is continuously growing and muography is under development toward its societal implementation in geophysical exploration,[28–35] in natural hazard assessment,[36–43] and in monitoring of industrial sites, infrastructures[44–48] as well as cultural heritages.[49–52] Concerning the assessment of flow hazards and mitigation of the corresponding sediment and flood catastrophes, muography has already been applied in the following case studies: Oláh et al. applied muography for monitoring the changes in deposited tephra on the ridge of Sakurajima volcano occurred due to post-eruptive lahars and water-driven erosion triggered by intense rainfalls.[53] Baccani et al. scanned the internal structure of river levees with cosmic-ray muons to reconstruct animal burrows and verified the observations with ERT and TLS.[54] Lázaro Roche et al. Monitored the water level from the downstream side of a reservoir dam.[55] Tanaka designed a muographic tide monitoring network and tested in the tunnel of the Tokyo Bay Aqua-Line.[56] In this work, we investigate the feasibility of SHM of debris dams via cosmic-ray muography.

RESULTS

Experimental setting

As the target of this study, we chose a sabo dam in the Katsuragawa River, Gunma prefecture, Japan. This is a debris dam made from mixture of rocks and concrete which is applied for erosion control of the river basin by means of sediment redemption.[57] The dam was built in 1951. It has a width of 67 m and height of 18 m Figure 1 shows a photograph about the inspected sabo dam and the surrounding site. Elastic wave tomography and drilling of dam structure were conducted by Tone River Basin Sabo Office of the Ministry of Land, Infrastructure, Transport and Tourism in 2011.[58] These surveys suggested the weakening of the right embankment body. As it is shown in two white rectangles in Figure 1, cement is releasing out from the embankment body at the downstream side in December 2020. The aim of measurement campaign was to test applicability of cosmic-ray muon imaging for detecting the weak regions in this dam. The black rectangle shows the inspected region of the dam in Figure 1. The topographic map of the measurement site is shown with a grid size of 1 m × 1 m in Figure 2. The observational instrument was installed at latitude of 36.437 N°, longitude of 138.684 E° and altitude above sea level of

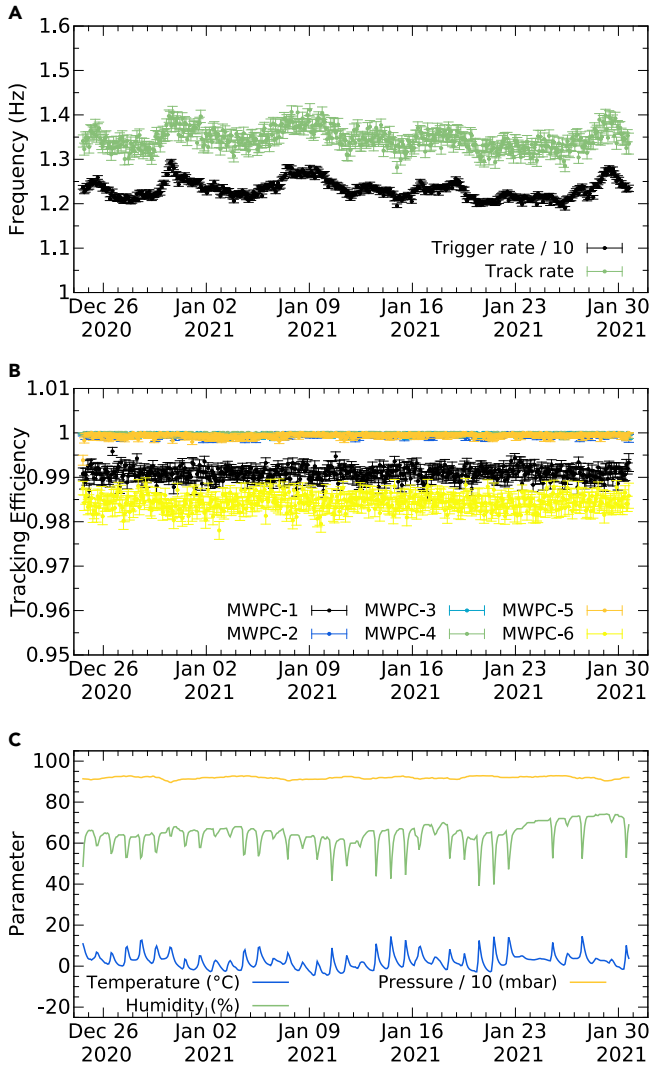

Figure 4. The time-line of main detector parameters and environmental parameters are plotted with a binning of 2 h during the data acquisition conducted from 24 December, 2020 until 2 February, 2021

(A) The trigger rate (black-colored error bars) and track rate (green-colored error bars) are shown in Hertz units.

(B) The tracking efficiencies are shown for MWPC-1, MWPC-2, MWPC-3, MWPC-4, MWPC-5, MWPC-6 with black, blue, light blue, green, orange, and yellow lines, respectively.

(C) The variations of temperature (blue line), humidity (green line) and pressure (orange line) measured in the detector box are shown.

819.6 m at a distance of 26.1 m from the downstream wall of the dam. The MOS was oriented to the azimuthal direction of 227° from north (black arrow) and tilted up 12.2° from the horizontal direction. It is worth noting that the detector could be installed to closer to this dam, however our aim was to conduct the surveying in a more realistic setting by taking into account the limited accessibility of other dams caused by topographic constraints.

We applied a multi-wire proportional chamber (MWPC)-based MOS for the muographic surveying of the sabo dam (see details in section experimental apparatus and Figure 3). We conducted the muographic surveying of the sabo dam from 24 December, 2020 until 2 February, 2021 with one technical stop that we performed on 12 January with a duration of a few minutes for replacement of the batteries and the gas bottle. The mountainous area did not allow to remotely access the tracking system during its operation because the mountains shielding of telephone network, thus we performed the analysis of the collected data after the technical stop and end of data acquisition (see details in section experimental procedure and Figures 4, 5, 6, 7, and 8).

Observational results

Figures 9A and 9B show the reconstructed density-lengths and averaged density-length errors through the dam and sediments. These quantities are shown as a function of horizontal distance measured from the observation axis of the muon detector and altitude above

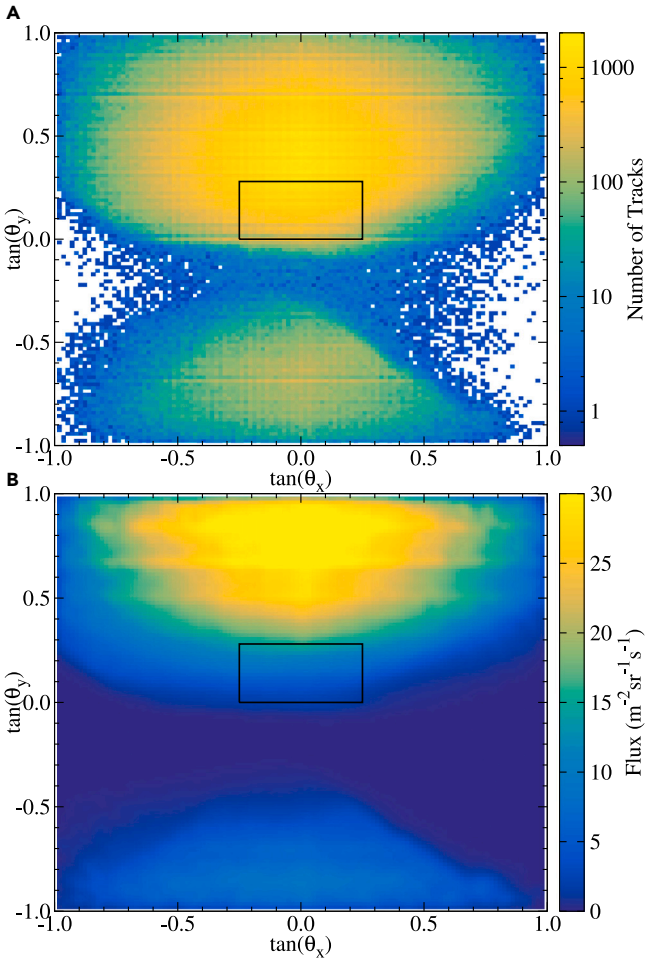

Figure 5. Directional dependent measurement of muons

The number of tracks (A) and the corresponding flux (B) are shown as a function of horizontal- and elevation track slopes. Black rectangles bound the inspected region of the dam.

sea level. The averaged density-length errors are determined via averaging the lower and upper density-length error values: $\Delta X_{ds} = (\Delta X_{ds,up} - \Delta X_{ds,low})/2$. The density-lengths and the averaged density-length errors ranged up to 25 hg cm^{-2} and 3 hg cm^{-2} in the region of interest. The average densities were determined based on Equation 3 for the dam. Figure 10A shows the muographic image with the density values. The densities ranged from 1.5 to 2.5 g cm^{-3} across the dam body, except at the region from which cement released from the embankment body (from horizontal distances from 2 m to 5 m and between the altitudes of 827 m and 830 m) where significantly lower density values (<1.5 g cm^{-3}) were observed. The densities were over-measured for the central part of the dam (see left from the horizontal coordinate of −4 m). The density values varied within a wide range between 0 g cm^{-3} and 4 g cm^{-3} for the ridge of the dam, where the path-lengths of muons were below 1 m. The muographically measured densities were compared to the densities that were determined via gamma-ray logging (see, e.g., in ref. [59]) along two boreholes in the dam by the Tone River Basin Sabo Office of the Ministry of Land, Infrastructure, Transport and Tourism in 2011.[58] Before the gamma-ray logging, mechanical boring was conducted in this region and samples were examined. The extracted samples revealed voids and cracks in this volume.[58] One of the boreholes was chosen to conduct of gamma-ray logging (see along the slice D of Figure 10A). The gamma-ray logging tool was equipped with[60] Co source that emitted gamma rays at a typical depth of 20–30 cm into the dam materials surrounding the borehole. The backscattered gamma rays were detected and the density of around the borehole was reconstructed with a vertical spatial resolution of 5 cm. The environmental effects (water level, natural radioactivity, etc.) on the measured gamma ray intensity resulted in a density correction of −0.255 g cm^{-3}. The bulk density of the dam was quantified to2.2 g cm $^{-3}$ along both boreholes. Based on this result, we assume this as a baseline density to the dam at all regions. Figures 10B–10D show comparison of muography (black dots with 1 standard deviation errors) and gamma-ray logging (dashed line) along three slices: (B) at one of the regions where cement released out from the embankment body, (C) at the axis of muographic observation, and (D) at the region where gamma-ray logging was conducted. Along the slices (B) and (C), the two different techniques provided densities with no significant differences. Along the slice (D), a significant difference was observed between the densities. While

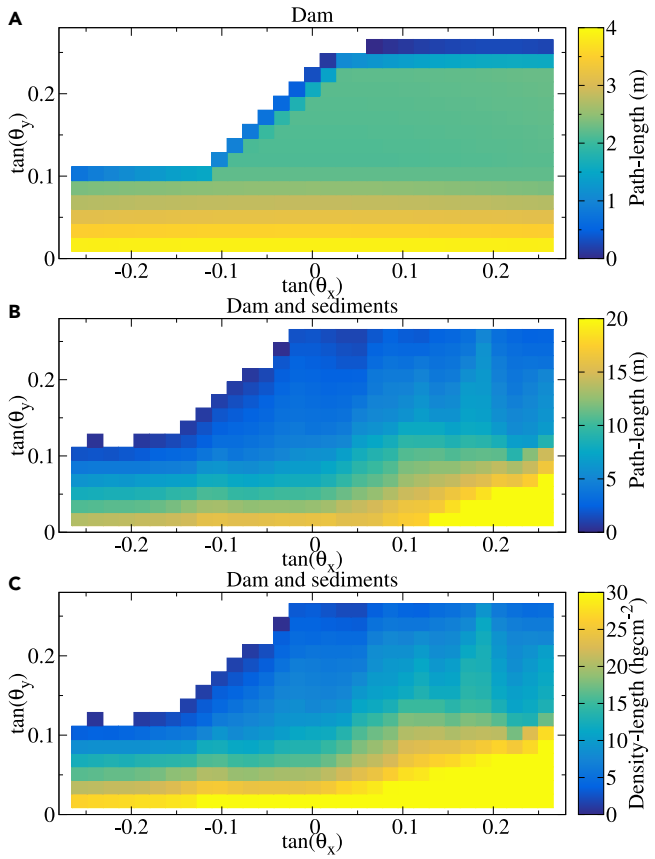

Figure 6. The path-length of muons were calculated from the center of the detector in an angular binning that is based on the horizontal- and vertical slopes

(A) The path-lengths are plotted for the dam structure located at the upstream side of the dam.

(B) The path-lengths are shown for the dam structure and the sediments.

(C) The expected density-lengths are plotted for the dam structure and sediments with the respectively density values of 2.3 g cm^{-3} and 1.8 g cm^{-3} in hg cm^{-2} (meter-water-equivalent) units.

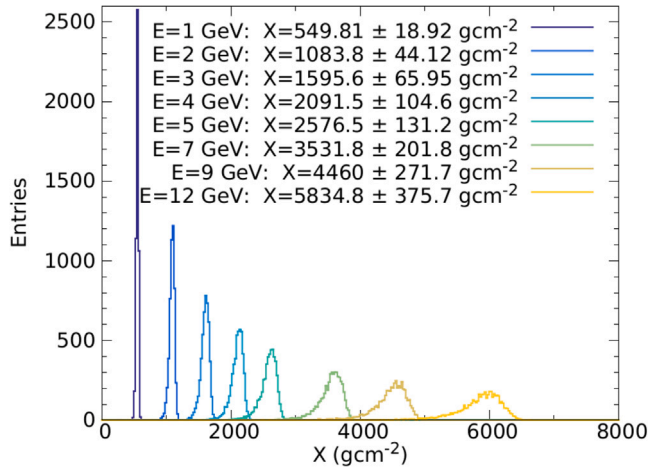

Figure 7. The distributions of the simulated energy ranges of muons in shielding concrete are shown for the energies of 1 GeV (dark blue histogram), 2 GeV (blue histogram), 3 GeV (light-blue histogram), 4 GeV (cyan histogram), 5 GeV (dark green histogram), 7 GeV (green histogram), 9 GeV (brown histogram), and 12 GeV (orange histogram)

The distributions are widening with the increase of energy due to the contributions of the stochastic energy loss processes to the total energy loss are higher for more energetic muons.

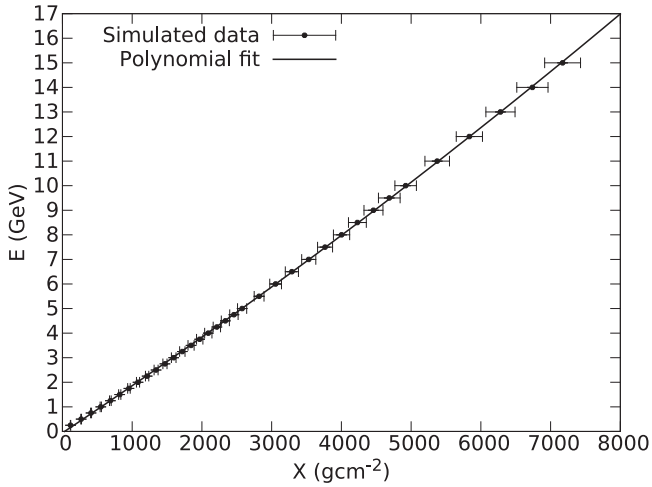

Figure 8. The minimum energies versus range in shielding concrete is shown by black error bars

A polynomial fitting (black line) was applied to determine the minimum muon energies required muons to penetrate across the dam (see the parameters in the text).

the gamma-ray logging is sensitive only to a depth up to a few tens of centimetres,[60] muography is sensitive up to a few kilometres.[26] The difference shown in Figure 10D might indicate that these two different techniques are looking at different depths, and this must be further studied in the future works e.g., by conducting joint inversion between muography and elastic wave tomography.

Figure 11 shows the map of the density differences in standard deviation units:$\sigma = (\rho_{d,logging} - \rho_{d,muon})/\Delta\rho_{d,muon}$. This image highlights a region with significant density decrease (<-5σ) at one of the regions from which cement released from the embankment body (see the right white rectangle in Figure 1). Other parts of the dam did not show such significant density differences, except along the crown of the dam where significant density increase was observed relative to the bulk density.

DISCUSSION

The progress in R&D of muography instrumentation allowed to apply portable devices for cosmic-ray muographic surveying of infrastructures in mountainous area. In this work, we conducted a remote, passive and non-destructive reconstruction of the density

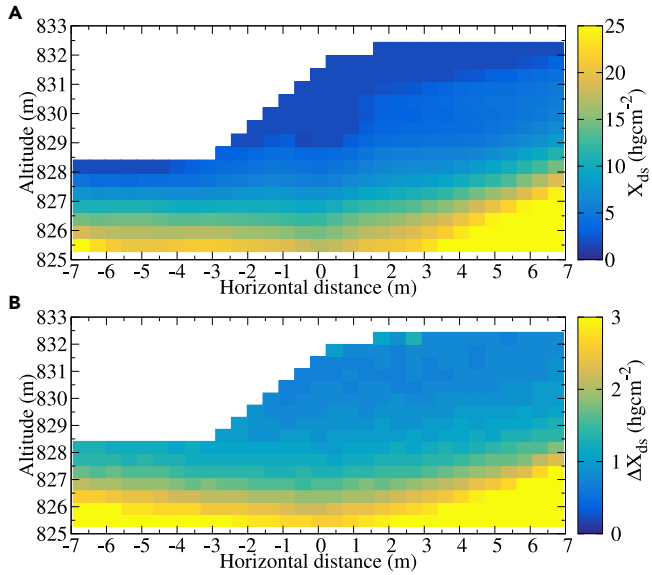

Figure 9. The density-lengths measured by muography

(A) The density-lengths are plotted for the dam and sediments located at the upstream side of the dam. (B) The averaged density-length errors are shown for the dam and sediments.

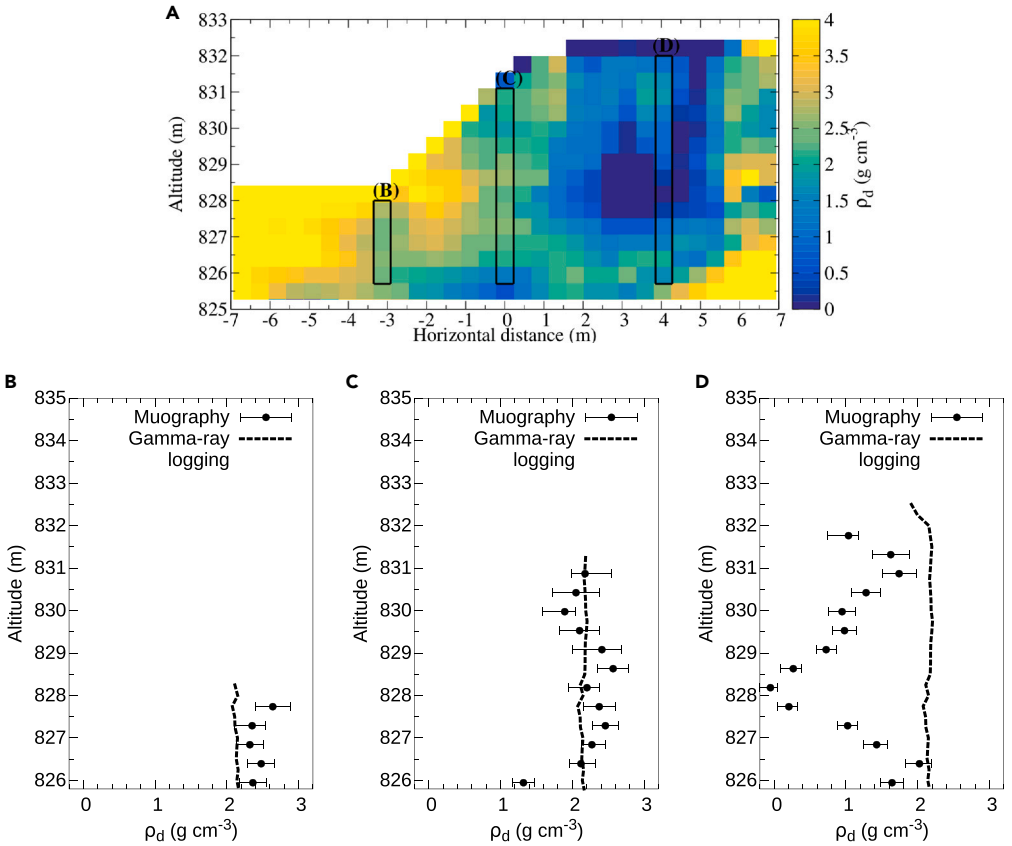

Figure 10. The averaged densities measured through the dam

(A–D) (A) The average-density values are shown as a function of horizontal distance and altitudes for the dam (see also in Figure 3B). Black rectangles highlight the location of vertical slices that are shown by black-colored error bars in panels (B), (C) and (D), respectively. Dashed lines show the densities measured by gamma-ray logging technique along the slice (D).

structure of a sabo dam with a spatial resolution of 0.5 m. The muographic observational results confirm the presence of a weak region inside the sabo dam where cement released out from the embankment body. This work demonstrates that cosmic-ray muography can serve useful complementary data to conventional techniques applied for SHM of debris dams. Further works, such as multi-directional measurements (see, e.g., in ref. [51,52]) or integrating muography with other density sensitive surveying technique, have to be done for accurate imaging targets with a thickness of a few meters and applying muography for the classification of structural quality of different parts of dams.

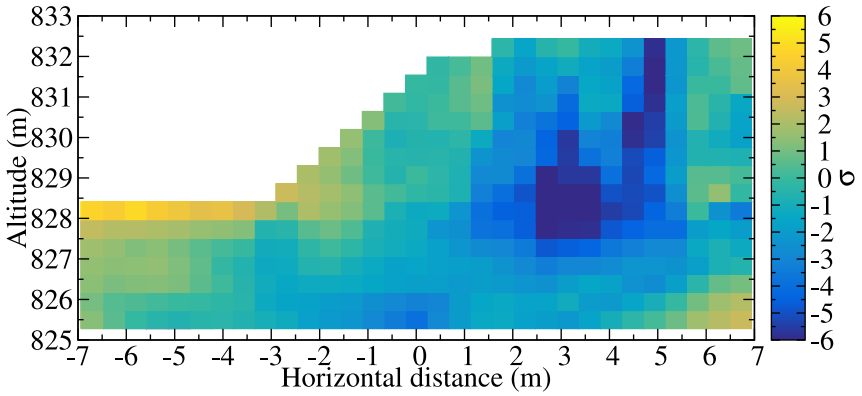

Figure 11. The density differences are shown in standard deviation (σ) units as a function of horizontal distance and altitudes for the dam

Limitations of the study

In this study, the spatial resolution was limited to 0.5 m. It could be improved via installing closer the instrument to the embankment body in this campaign, however it would not be possible at other check dams. Muography did not reveal significant density decrease for another weak region (see within the left white rectangle in Figure 1). Smaller volume and shorter vertical extension of the weak region did not exceed the spatial resolution, thus spatial resolution limited the applicability for inspecting this region. Furthermore, muography overestimated the density for the crown part of the dam where the path-lengths do not exceed 1 m. This is assumed to be a result of systematic errors introduced by two factors: (1) the uncertainty of the path-lengths due to the finite (1 m × 1 m) segmentation of digital elevation data and (2) inaccurate modeling of the angular dependent energy spectra of cosmic-ray muons at smaller energies due to the spare experimental data.

Concerning the role of muography for SHM of debris dams, the finite yield of muons limits the duration of surveying to a few weeks for targets with typical thicknesses ranges up to a few tens of meters. The accessibility (e.g., some sites are hard to reach to install the instrument) and topography (e.g., larger amount of rock mass located behind the dam) of the measurement sites and the possibility of flooding can limit the applicability of this technique. The power consumption of current real-time muography instruments (e.g., 6 W for MWPC-based tracking systems) limits the time of autonomous operation for a few weeks. Nuclear emulsion technology can overcome on the aforementioned technical issues of real-time detectors and it is a good candidates at many sites.[61] However, it also has a few limitations, e.g., it operates reliably in an environment with a typical temperature above 25°C, it does not provide timing information to the recorded tracks, etc. Therefore, muon detector technology has to be chosen based on the local environmental conditions and purpose of surveying.

STAR★METHODS

Detailed methods are provided in the online version of this paper and include the following:

- KEY RESOURCES TABLE
- RESOURCE AVAILABILITY
  - Lead contact
  - Materials availability
  - Data and code availability
- EXPERIMENTAL MODEL AND STUDY PARTICIPANT DETAILS
- METHOD DETAILS
  - Material preparation
  - Experimental apparatus
- EXPERIMENTAL PROCEDURE
  - Analysis methods
  - Simulation methods
- QUANTIFICATION AND STATISTICAL ANALYSIS
- ADDITIONAL RESOURCES

ACKNOWLEDGMENTS

This work was supported by the Joint Usage Research Project (JURP) of the University of Tokyo, Earthquake Research Institute, University of Tokyo (ERI) under project ID 2023-H-03, the Hungarian NKFIH research grants under identification numbers OTKA-FK-135349 and TKP2021-NKTA-10 and the Ministry of Education, Culture, Sports, Science and Technology, Japan (MEXT) Integrated Program for the Next Generation Volcano Research; and the INTENSE H2020 MSCA RISE, GA No. 822185.

AUTHOR CONTRIBUTIONS

L.O., T.M., Y.S., H.K.M.T., and D.V. designed the experiment. D.V. and L.O. developed the instrumentation. Y.S., T.M., and L.O. conducted the experiment. L.O. analyzed the data. L.O., T.M., and Y.S. interpreted the data. L.O. wrote and revised the paper.

DECLARATION OF INTERESTS

The authors declare no competing interests.

Received: May 17, 2023
Revised: July 14, 2023
Accepted: September 19, 2023
Published: September 22, 2023

REFERENCES

1. Iverson, R.M. (1997). The physics of debris flows. Rev. Geophys. *35*, 245–296. https://doi.org/10.1029/97RG00426.
2. Iverson, R.M., Reid, M.E., Logan, M., LaHusen, R.G., Godt, J.W., and Griswold, J.P. (2011). Positive feedback and momentum growth during debris-flow entrainment of wet bed sediment. Nat. Geosci. *4*, 116–121. https://doi.org/10.1038/ngeo1040.
3. de Haas, T., Nijland, W., de Jong, S.M., McArdell, B.W., and McArdell, B.W. (2020). How memory effects, check dams, and channel geometry control erosion and deposition by debris flows. Sci. Rep. *10*, 14024. https://doi.org/10.1038/s41598-020-71016-8.
4. Dowling, C.A., and Santi, P.M. (2014). Debris flows and their toll on human life: a global analysis of debris-flow fatalities from 1950 to 2011. Nat. Hazards *71*, 203–227. https://doi.org/10.1007/s11069-013-0907-4.
5. Garcia-Martinez, R., and Lopez, J.L. (2005). Debris flows of December 1999 in Venezuela. In Debris-flow hazards and related phenomena, O. Hungr and M. Jakob, eds. (Springer-Praxis), pp. 519–538.
6. Turkington, T., Remaître, A., Ettema, J., Hussin, H., and van Westen, C. (2016). Assessing debris flow activity in a changing climate. Climatic Change *137*, 293–305. https://doi.org/10.1007/s10584-016-1657-6.
7. Vagnon, F. (2020). Design of active debris flow mitigation measures: a comprehensive analysis of existing impact models. Landslides *17*, 313–333. https://doi.org/10.1007/s10346-019-01278-5.
8. Zanchetta, G., Sulpizio, R., Pareschi, M.T., Leoni, F.M., and Santacroce, R. (2004). Characteristics of 2004 volcaniclastic debris flows in the Sarno area (Campania, southern Italy): relationships to structural damage and hazard zonation. J. Volcanol. Geoth. Res. *133*, 377–393. https://doi.org/10.1016/S0377-0273(03)00409-8.
9. Itakura, Y., Inaba, H., and Sawada, T. (2005). A debris-flow monitoring devices and methods bibliography, Nat. Hazards Earth Syst. Sci. *5*, 971–977. https://doi.org/10.5194/nhess-5-971-2005.
10. Hürlimann, M., Coviello, V., Bel, C., Guo, X., Berti, M., Graf, C., Hübl, J., Miyata, S., Smith, J.B., and Yin, H.-Y. (2019). Debris-flow monitoring and warning: Review and examples. Earth Sci. Rev. *199*, 102981. https://doi.org/10.1016/j.earscirev.2019.102981.
11. Rickenmann, D. (2016). Debris-Flow Hazard Assessment and Methods Applied in Engineering Practice. International Journal of Erosion Control Engineering *9*, 80–90. https://doi.org/10.13101/ijece.9.80.
12. Mizuyama, T. (2008). Structural Countermeasures for Debris Flow Disasters. International Journal of Erosion Control Engineering *1*, 38–43. https://doi.org/10.13101/ijece.1.38.
13. Remaître, A., van Asch, T.W.J., Malet, J.P., and Maquaire, O. (2008). Influence of check dams on debris-flow run-out intensity. Nat. Hazards Earth Syst. Sci. *8*, 1403–1416. Th. https://doi.org/10.5194/nhess-8-1403-2008.
14. Chen, X., Wang, F.Y., Chu, G.J., Zhu, Y.F., Tan, H.W., Zhao, X.X., Qin, Y.W., and Ge, J.B. (2015). Engineering measures for debris flow hazard mitigation in the Wenchuan earthquake area. Eng. Geol. *1*, 73–80. https://doi.org/10.1016/j.enggeo.2014.10.002.
15. Chanson, H. (2004). Sabo check dams – mountain protection systems in Japan. Intl. J. River Basin Management *2*, 301–307. https://doi.org/10.1080/15715124.2004.9635240.
16. Piton, G., Carladous, S., Recking, A., Tacnet, J.M., Liébault, F., Kuss, D., Quefféléan, Y., and Marco, O. (2016). Why do we build check dams in Alpine streams? Anhistorical perspective from the French experience. Earth Surf. Process. Landforms *42*, 91–108. https://doi.org/10.1002/esp.3967.
17. Bukenya, P., Moyo, P., Beushausen, H., and Oosthuizen, C. (2014). Health monitoring of concrete dams: a literature review. J. Civil Struct. Health Monit. *4*, 235–244. https://doi.org/10.1007/s13349-014-0079-2.
18. Hanna, A.W., Plewes, H.D., Wong, R., and Seyers, W.C. (1993). Investigations of high uplift pressures beneath a concrete dam. Can. Geotech. J. *30*, 974–990. https://doi.org/10.1139/t93-095.
19. Kronenberg, P., Casanova, N., Inaudi, D., and Vurpillot, S. (1997). Dam monitoring with fiber optics deformation sensors. Proc. SPIE 3043, Smart Structures and Materials, 1997, Smart Systems for Bridges, Structures, and Highways *1997*, 1–11. https://doi.org/10.1117/12.274637.
20. Alba, M., Fregonese, L., Prandi, F., Scaioni, M., and Valgoi, P. (1998). Structural Monitoring of a Large Dam by Terrestrial Laser Scanning. https://www.isprs.org/proceedings/XXXVI/part5/paper/1271_Dresden06.pdf.
21. Behr, J.A., Hudnut, K.W., and King, N.E. (1998). Monitoring Structural Deformation at Pacoima Dam, California Using Continuous GPS. Proceedings of the 11th International Technical Meeting of the Satellite Division of the Institute of Navigation, pp. 59–68. https://www.ion.org/publications/abstract.cfm?articleID=2934.
22. Tarchi, D., Rudolf, H., Luzi, G., Chiarantini, L., Coppo, P., and Sieber, A.J. (2016). SAR interferometry for structural changes detection: a demonstration test on a dam. In Proceedings of the IEEE International Geoscience and Remote Sensing Symposium (IGARSS 99), *3*, pp. 1522–1524. https://doi.org/10.1109/IGARSS.1999.772006.
23. Kang, F., Li, J., Zhao, S., and Wang, Y. (2019). Structural health monitoring of concrete dams using long-term air temperature for thermal effect simulation. Eng. Struct. *180*, 642–653. https://doi.org/10.1016/j.engstruct.2018.11.065.
24. Kisanuki, H., Aoike, K., Saito, H., Inazaki, T., Shimizu, T., Izumiyama, H., and Fujimura, N. (2015). Fracture Imaging of a Sabo Dam Damaged by a Debris Flow by Means of GPR and High-Resolution Seismic Survey, Proceedings of the 12th SEGJ International Symposium, Tokyo, Japan. https://doi.org/10.1190/segj122015-050.
25. Loperte, A., Soldovieri, F., Palombo, A., Santini, F., and Lapenna, V. (2016). An integrated geophysical approach for water infiltration detection and characterization at Monte Cotugno rock-fill dam (southern Italy). Eng. Geol. *211*, 162–170. https://doi.org/10.1016/j.enggeo.2016.07.005.
26. Oláh, L., Tanaka, H.K.M., and Varga, D. (2022). Muography: exploring earth subsurface with elementary particles, American Geophysical Union. Geophys. Monogr. *270*, 9781119723028. https://doi.org/10.1002/9781119722748.
27. Scampoli, P., and Ariga, A. (2023). Cosmic Ray Muography. World Scientific9789811264900. https://doi.org/10.1142/13102.
28. Schouten, D. (2018). Muon geotomography: selected case studies. Phil. Trans. R. Soc. A *377*, 20180061. https://doi.org/10.1098/rsta.2018.0061.
29. Holma, M., Zhang, Z., Kuusiniemi, P., Loo, K., and Enqvist, T. (2022). Future Prospects of Muography for Geological Research and Geotechnical and Mining Engineering. Gephysical Monograph Series *270*, 199–219. https://doi.org/10.1002/9781119722748.ch15.
30. Oláh, L., Barnaföldi, G.G., Hamar, G., Melegh, H.G., Surányi, G., and Varga, D. (2012). CCC-based muon telescope for examination of natural caves. Geosci. Instrum. Method. Data Syst. *1*, 229–234. https://doi.org/10.5194/gi-1-229-2012.
31. Cimmino, L., Baccani, G., Noli, P., Amato, L., Ambrosino, F., Bonechi, L., Bongi, M., Ciulli, V., D'Alessandro, R., D'Errico, M., et al. (2019). 3D Muography for the Search of Hidden Cavities. Sci. Rep. *9*, 2974. https://doi.org/10.1038/s41598-019-39682-5.
32. Tanaka, H.K., Miyajima, H., Kusagaya, T., Taketa, A., Uchida, T., and Tanaka, M. (2011). Cosmic muon imaging of hidden seismic fault zones: Rainwater permeation into the mechanical fracture zone in Itoigawa-Shizuoka Tectonic Line, Japan, Earth Planet. Sc. Lett. *306*, 156–162. https://doi.org/10.1016/j.epsl.2011.03.036.
33. Beni, T., Borselli, D., Bonechi, L., Bongi, M., Brocchini, D., Ciaranfi, R., Cimmino, L., Ciulli, V., D'Alessandro, R., Dini, A., et al. (2023). Transmission-Based Muography for Ore Bodies Prospecting: A Case Study from a Skarn Complex in Italy, Nat. Resour. Res. *32*, 1529–1547. https://doi.org/10.1007/s11053-023-10201-8.
34. Lázaro Roche, I., Pasquet, S., Chalikakis, K., Mazzilli, N., Rosas-Carbajal, M., Decitre, J.-B., Serene, L., Batiot-Guilhe, C., Emblanch, C., Marteau, J., and Gaffet, S. (2022). The Multi-Technique Approach of the Low Background Noise Underground Research Laboratory and its Muon Detection Projects,. Geophys. Monogr. *270*, 137–152. https://doi.org/10.1002/9781119722748.ch10.
35. Taketa, A., Nishiyama, R., Yamamoto, K., and Iguchi, M. (2022). Radiography using cosmic-ray electromagnetic showers and its application in hydrology. Sci. Rep. *12*, 20395. https://doi.org/10.1038/s41598-022-24765-7.
36. Tanaka, H.K.M., and Muraoka, H. (2013). Interpreting muon radiographic data in a fault zone: possible application to geothermal reservoir detection and monitoring. Geosci. Instrum. Method. Data Syst. *2*, 145–150. https://doi.org/10.5194/gi-2-145-2013.

37. Miyamoto, S., Barrancos, J., Bozza, C., Consiglio, L., De Sio, C., Hernández, P., Nishiyama, R., Padilla, G., Padrón, E., Sirigano, C., et al. (2017). Muography of 1949 fault in La Palma, Canary Islands, Spain. Ann. Geophys. *60*, S0110. https://doi.org/10.4401/ag-7385.
38. Yamazaki, K., Taketa, A., Ikeda, D., and Omura, K. (2022). Development of detector and method for density structure measurement of fault zones using cosmic ray muons, Nucl. Inst. Meth. Phys. Res. A *1031*, 166518. https://doi.org/10.1016/j.nima.2022.166518.
39. Tanaka, H.K.M. (2018). Japanese volcanoes visualized with muography. Phil. Trans. R. Soc. A *377*, 20180142. https://doi.org/10.1098/rsta.2018.0142.
40. Rosas-Carbajal, M., Jourde, K., Marteau, J., Deroussi, S., Komorowski, J.-C., and Gibert, D. (2017). Three-dimensional density structure of La Soufrière de Guadeloupe lava dome from simultaneous muon radiographies and gravity data. Geophys. Res. Lett. *44*, 6743–6751. https://doi.org/10.1002/2017GL074285.
41. Tioukov, V., Alexandrov, A., Bozza, C., Consiglio, L., D'Ambrosio, N., De Lellis, G., De Sio, C., Giudicepietro, F., Macedonio, G., Miyamoto, S., et al. (2019). First muography of Stromboli volcano. Sci. Rep. *9*, 6695. https://doi.org/10.1038/s41598-019-43131-8.
42. Lo Presti, D., Riggi, F., Ferlito, C., Bonanno, D.L., Bonanno, G., Gallo, G., La Rocca, P., Reito, S., and Romeo, G. (2020). Muographic monitoring of the volcano-tectonic evolution of Mount Etna. Sci. Rep. *10*, 11351. https://doi.org/10.1038/s41598-020-68435-y.
43. Nishiyama, R., Ariga, A., Ariga, T., Käser, S., Lechmann, A., Mair, D., Scampoli, P., Vladymyrov, M., Ereditato, A., and Schlunegger, F. (2017). First measurement of ice-bedrock interface of alpine glaciers by cosmic muon radiography. Geophys. Res. Lett. *44*, 6244–6251. https://doi.org/10.1002/2017GL073599.
44. Gluyas, J., Thompson, L., Allen, D., Benton, C., Chadwick, P., Clark, S., Klinger, J., Kudryavtsev, V., Lincoln, D., Maunder, B., et al. (2018). Passive, continuous monitoring of carbon dioxide geostorage using muon tomography. Phil. Trans. R. Soc. A *377*, 20180059. https://doi.org/10.1098/rsta.2018.0059.
45. Thompson, L.F., Stowell, J.P., Fargher, S.J., Steer, C.A., Loughney, K.L., O'Sullivan, E.M., Gluyas, J.G., Blaney, S.W., and Pidcock, R.J. (2020). Muon tomography for railway tunnel imaging. Phys. Rev. Research *2*, 023017. https://doi.org/10.1103/PhysRevResearch.2.023017.
46. Marteau, J., de Bremond d'Ars, J., Carlus, B., Chevalier, A., Cohu, A., Descombes, T., Gibert, D., Ianigro, J., Jourde, K., Kergosien, B., et al. (2022). Development of Scintillator-Based Muon Detectors for Muography. Geophys. Monogr. *270*, 237–252. https://doi.org/10.1002/9781119722748.ch17.
47. Oláh, L., Hamar, G., Miyamoto, S., Tanaka, H.K.M., and Varga, D. (2018). The first prototype of an MWPC-based borehole-detector and its application for muography of an underground pillar,. Butsuri-Tansa *71*, 161–168. https://doi.org/10.3124/segj.71.161.
48. Niederleithinger, E., Gardner, S., Kind, T., Kaiser, R., Grunwald, M., Yang, G., Redmer, B., Waske, A., Mielentz, F., Effner, U., et al. (2021). Muon Tomography of the Interior of a Reinforced Concrete Block: First Experimental Proof of Concept. J. Nondestr. Eval. *40*, 65. https://doi.org/10.1007/s10921-021-00797-3.
49. Morishima, K., Kuno, M., Nishio, A., Kitagawa, N., Manabe, Y., Moto, M., Takasaki, F., Fujii, H., Satoh, K., Kodama, H., et al. (2017). Discovery of a big void in Khufu's Pyramid by observation of cosmic-ray muons. Nature *552*, 386–390. https://doi.org/10.1038/nature24647.
50. Guardincerri, E., Bacon, J.D., Barros, N., Blasi, C., Bonechi, L., Chen, A., D'Alessandro, R., Durham, J.M., Fine, M., Mauger, C., et al. (2018). Imaging the dome of Santa Maria del Fiore using cosmic rays, Philos. T. R. Soc. A *377*, 20180136. https://doi.org/10.1098/rsta.2018.0136.
51. Tanaka, H.K.M., Sumiya, K., and Oláh, L. (2020). Muography as a new tool to study the historic earthquakes recorded in ancient burial mounds. Geosci. Instrum. Method. Data Syst. *9*, 357–364. https://doi.org/10.5194/gi-9-357-2020.
52. Liu, G., Luo, X., Tian, H., Yao, K., Niu, F., Jin, L., Gao, J., Rong, J., Fu, Z., Kang, Y., et al. (2023). High-precision muography in archaeogeophysics: A case study on Xi'an defensive walls,. J. Appl. Phys. *133*. https://doi.org/10.1063/5.0123337.
53. Oláh, L., Tanaka, H.K.M., and Hamar, G. (2021). Muographic monitoring of hydrogeomorphic changes induced by post-eruptive lahars and erosion of Sakurajima volcano. Sci. Rep. *11*, 17729. https://doi.org/10.1038/s41598-021-96947-8.
54. Baccani, G., Bonechi, L., Bongi, M., Casagli, N., Ciaranfi, R., Ciulli, V., D'Alessandro, R., Gonzi, S., Lombardi, L., Morelli, S., et al. (2021). The reliability of muography applied in the detection of the animal burrows within River Levees validated by means of geophysical techniques. J. Appl. Geophys. *191*, 104376. https://doi.org/10.1016/j.jappgeo.2021.104376.
55. Lázaro Roche, I., Bitri, A., Bouteille, S., Decitre, J.-B., Jourde, K., Gance, J., Truffert, C., and Gaffet, S. (2019). Design, Construction and In Situ Testing of a Muon Camera for Earth Science and Civil Engineering Applications. E3S Web Conf. *88*, 01003. https://doi.org/10.1051/e3sconf/20198801003.
56. Tanaka, H.K.M. (2022). Muography for a dense tide monitoring network. Sci. Rep. *12*, 6725. https://doi.org/10.1038/s41598-022-10373-y.
57. Last view on 3 July 2023. https://geolog.mydns.jp/1st.geocities.jp/guntatetan/10–0171.html.
58. Tone River Basin Sabo Office; Ministry of Land, Infrastructure Transport and Tourism (2011). Report about the structural surveying of Karasugawa sabo dam (In Japanese).
59. Wahl, J.S. (1983). Gamma-ray logging. Geophysics *48*, 1536–1550. https://doi.org/10.1190/1.1441436.
60. Mahmoud, K.A., Sayyed, M.I., and Tashlykov, O.L. (2019). Gamma ray shielding characteristics and exposure buildup factor for some natural rocks using MCNP-5 code. Nucl. Eng. Technol. *51*, 1835–1841. https://doi.org/10.1016/j.net.2019.05.013.
61. Kitagawa, N. (2023). Application of Muography with Nuclear Emulsions for the Observation inside Levees (Muographers Workshop). https://indico.cern.ch/event/1203839/contributions/5332753/.
62. Varga, D., Gál, Z., Hamar, G., Sára Molnár, J., Oláh, É., and Pázmándi, P. (2015). Cosmic muon detector using proportional chambers. Eur. J. Phys. *36*, 065006. https://doi.org/10.1088/0143-0807/36/6/065006.
63. Varga, D., Nyitrai, G., Hamar, G., and Oláh, L. (2016). High Efficiency Gaseous Tracking Detector for Cosmic Muon Radiography. Adv. HEP *2016*, 1–11. https://doi.org/10.1155/2016/1962317.
64. Varga, D., J Balogh, S., Gera, Á., Hamar, G., Nyitrai, G., Suranyi, G., Nyitrai, G., and Surányi, G. (2022). Construction and Readout Systems for Gaseous Muography Detectors. Journal of Advanced Instrumentation in Science *2022*, JAIS-307. https://doi.org/10.31526/jais.2022.307.
65. Gera, Á., Nyitrai, G., Surányi, G., Surányi, G., Varga, D., and Varga, D. (2022). Gaseous Detectors for Field Applications: Quality Control, Thermal and Mechanical Stability. Instruments *6*, 74. https://doi.org/10.3390/instruments6040074.
66. Nyitrai, G., Hamar, G., and Varga, D. (2021). Towards low gas consumption of muographic tracking detectors in field applications. J. Appl. Phys. *129*. https://doi.org/10.1063/5.0053984.
67. Oláh, L. (2016). Research and Development of Particle Detectors for Muon Tomography and the CERN ALICE Experiment. CERN-THESIS-2017-085 (Eötvös Loránd University). https://doi.org/10.15476/ELTE.2016.144.
68. Surányi, G., Hamar, G., Nyitrai, G., and Gera, Á. (2022). Application examples of underground muography. EGU General Assembly *2022*. EGU22–3551. https://doi.org/10.5194/egusphere-egu22-3551.
69. Oláh, L., Tanaka, H.K.M., Ohminato, T., and Varga, D. (2018). High-definition and low-noise muography of the Sakurajima volcano with gaseous tracking detectors. Sci. Rep. *8*, 3207. https://doi.org/10.1038/s41598-018-21423-9.
70. Sagisaka, S. (1986). Atmospheric effects on cosmic-ray muon intensities at deep underground depths. Il Nuovo Cimento *9*, 809–828. https://doi.org/10.1007/BF02558081.
71. Pagano, D., Bonomi, G., Donzella, A., Zenoni, A., Zumerle, G., and Zurlo, N. (2021). EcoMug: An Efficient COsmic MUon Generator for cosmic-ray muon applications. Nucl. Inst. Meth. Phys. Res. A *1014*, 165732. https://doi.org/10.1016/j.nima.2021.165732.
72. Bonechi, L., Bongi, M., Fedele, D., Grandi, M., Ricciarini, S., and Vannuccini, E. (2005). Development of the ADAMO detector: test with cosmic rays at different zenith angles. 29th International Cosmic Ray Conference *9*, 283. https://adsabs.harvard.edu/full/2005ICRC....9..283B.
73. Cecchini, S., and Spurio, M. (2012). Atmospheric muons: experimental aspects. Geosci. Instrum. Method. Data Syst. *1*,

185–196. https://doi.org/10.5194/gi-1-185-2012.

74. Lesparre, N., Gibert, D., Marteau, J., Déclais, Y., Carbone, D., and Galichet, E. (2010). Geophysical muon imaging: feasibility and limits. Geophys. J. Int. *183*, 1348–1361. https://doi.org/10.1111/j.1365-246X.2010.04790.x.
75. Oláh, L., Tanaka, H.K.M., Suenaga, H., Miyamoto, S., Galgóczi, G., Hamar, G., and Varga, D. (2022). Development of Machine Learning-Assisted Spectra Analyzer for the NEWCUT Muon Spectrometer. Journal of Advanced Instrumentation in Science *2022*, JAIS-264. https://doi.org/10.31526/JAIS.2022.264.
76. Agostinelli, S., Allison, J., Amako, K., Apostolakis, J., Araujo, H., Arce, P., Asai, M., Axen, D., Banerjee, S., Barrand, G., et al. (2003). Geant4 – a simulation toolkit. Nucl. Instr. Meth. A *506*, 250–303. https://doi.org/10.1016/S0168-9002(03)01368-8.
77. Lechmann, A., Mair, D., Ariga, A., Ariga, T., Ereditato, A., Nishiyama, R., Pistillo, C., Scampoli, P., Schlunegger, F., and Vladymyrov, M. (2018). The effect of rock composition on muon tomography measurements. Solid Earth *9*, 1517–1533. https://doi.org/10.5194/se-9-1517-2018.

STAR★METHODS

KEY RESOURCES TABLE

REAGENT or RESOURCE	SOURCE	IDENTIFIER
Batteries	RENOGY	https://www.renogy.com/template/files/Specifications/BATT-LFP-12-100.pdf

RESOURCE AVAILABILITY

Lead contact

Further information and requests for resources should be directed to and will be fulfilled by the lead contact, László Oláh (olah.laszlo@wigner.hu). Requests for raw digital elevation model data, geometric data of the sabo dam, raw gamma-ray logging data and ref.[58] should be directed to Sabo Frontier Foundation (Yukihiko Sakatani, y.sakatani@sff.or.jp).

Materials availability

This study did not generate new unique reagents.

Data and code availability

- The datasets used and/or analyzed during the current study available from the lead contact on reasonable request.
- This paper does not report original codes.
- Any additional information required to reanalyze the data reported in this paper is available from the lead contact upon request.

EXPERIMENTAL MODEL AND STUDY PARTICIPANT DETAILS

Our study does not use experimental models typical in the life sciences.

METHOD DETAILS

Material preparation

Our study does not materials typical in the life sciences.

Experimental apparatus

The detailed design of the MWPC technology is discussed extensively by Varga et al. in ref.[62–65] It is a high-performance gaseous detector that is utilized for tracking of the charged particles penetrated across its sensitive volume. Electric signal is produced by means of ionization of gas atoms by charged particles that penetrated across the sensitive volume. The MWPCs are flushed with environmental friendly (non-flammable and non-toxic) industrial gas mixture with Ar and CO 2 gases in a respectively proportion of 80% and 20% for signal production.[66] The key element of the detector design is two perpendicular wire planes with a distance of 12 mm that allows to localize particles' positions with a resolution of approx. 12 mm/$\sqrt{12}$.[63] A combination of microcomputer-based data acquisition system and custom designed electronics allows remote operation for the tracking system. Furthermore, the application of a custom designed temperature-humidity-pressure (TPH) sensor allows to monitoring the changes of environmental conditions both inside and outside of detector housing during the data acquisition in parallel with collecting tracking data. Data collection is triggered by the coincidence of MWPCs and the acquired data is written into ASCII files on event-by-event. The data readout process causing a dead time in order of 100 μs that result in negligible (<0.6%) loss of events under open sky.[67] The light-weight detector elements (e.g., the mass of an MWPC with a size of 40 cm × 40 cm is 2.7 kg) allows to us to design portable systems that can be applied at remote locations, such as underground tunnels or caves.[67,68] For muographic surveying the sabo dam, we applied 40 cm × 40 cm-sized MWPC detectors. We designed a plexiglass housing for the tracking system that allowed to install it in mountainous area which has sometimes limited accessibility due to the topography. Six MWPCs were arranged vertically into the box within a horizontal distance of 36 cm that allowed an opening angle of 47.2° in both of horizontal and vertical directions. Figure 3 shows a photograph about the installation of the tracking system at the downstream side of the sabo dam. We applied a gas bottle with a volume of 10 litres and pressure of 130 bar for supplying the tracking system. The gas mixture was flushed with flow of 2 litres per hour through through the MWPCs. We applied two standard 100 Ah batteries for supplying power to the tracking system with +12 V DC.

EXPERIMENTAL PROCEDURE

Analysis methods

The analysis chain is based on two main procedures: (1) an event-by-event procedure reconstructs the tracks of the detected charged particles, (2) a method for calculating of the flux of selected tracks. The track reconstruction is performed independently in the horizontal and

the vertical directions. The procedure initiates with cluster reconstruction. This determines the continuous sequences of wires via calculating the positions of centroids, sizes and numbers on each detector. Thereafter, track candidates are reconstructed by a combinatorial algorithm which is based on linear fitting. The slopes (tangents of horizontal (θ_x) and vertical (θ_y) angles), the intercepts, and the goodness of the fit are determined for each track. The track candidates are sorted and the best fitting

one is chosen based on the "goodness" of the fit, one is chosen based on the "goodness" of the fit, $\chi^2_{x,y}$/NDF, which is defined by the following equation.

$$\chi^2_{x,y} = \Sigma_{i = 1:Ndet} \left[\left(z_{measured,i} - z_{fitted,i}\right)^2 \Big/ \sigma^2_{det,i} \right] \quad \text{(Equation 1)}$$

where $z_{measured,i}$ is the reconstructed cluster centroids, $z_{fitted,i}$ is the intersection of the fitted straight track on the given detector layer, $\sigma_{det,i} \approx \sigma_{MWPC}$ is the position resolution of the MWPCs, and$N_{det} = 6$ is the number of detectors in the tracking system. The efficiency of tracking was also calculated on detector-by-detector basis by a similar algorithm.[69] In the first step, it chooses a specific detector and reconstructs the trajectory of the particle from the other chambers excluding the detector under study. If there is straight track, then the algorithm checks the presence of a cluster within a fiducial zone (typically two detector segments) around the extrapolated coordinate in the investigated chamber. The tracking efficiency is the number of cases when there was cluster divided by the number of extrapolations.

The track reconstruction algorithm allows to conduct quality assurance of the data before the flux calculation. Figures 4A–4C show the variations of the main parameters of detector performance and environmental parameters with a time bin size of 2 hours for the period from 24 December 2020 until 2 February 2021. The frequency of triggers (triple coincidence of MWPCs, shown by black error bars) shows moderate variations of below 5% and demonstrates that the tracking system operate without significant noise that could affect the muographic surveying. The frequency of tracks (green error bars) show variations of below 2.5% during the data collection period mainly due to atmospheric pressure changes which affect the production of muons.[70] The tracking efficiencies were found above 98% for each of the six MWPCs. The efficiency of measuring track coordinates on five out six MWPCs approached the efficiency of 100%.

The angular dependent quantities were determined in the "natural" coordinate system of the tracking system that is based on the slopes of the reconstructed tracks. Therefore, the muon flux (F) was calculated for each $\Delta\tan(\theta_x)$ - $\Delta\tan(\theta_y)$ bin as follows.

$$F = N / (A \times \Omega \times T) \quad \text{(Equation 2)}$$

where N is the number of tracks that have χ^2/NDF = $\sqrt{(\chi^2_x + \chi^2_y)}$/NDF <1.25, the A is the detector acceptance, the Ω is the covered solid angle and T is the duration of data acquisition.[67] Figure 5A shows the track counts in $\Delta\tan(\theta_x)$-$\Delta\tan(\theta_y)$ angular bins. The corresponding flux is shown in Figure 5B. Both track count and flux values reflect the topography of the measurement site: the smaller fluxes and the horizontal asymmetry for negative vertical slopes is observed due the presence of a rock wall behind the tracking system that absorb relatively more muons. These images demonstrate that muography is applicable to scan a large volume even from a single measurement point and capable to inspect the structure of large dams (see also in ref. [55]). The black rectangle highlight the region of interest of this study (see within the black rectangle in Figure 1) where the presence of weak regions was expected. In the next sections, we will focus on this selected region.

Simulation methods

Muography reconstructs the average density-length (density integrated along path of muons, X_{ds}) through the dam and the sedimented materials for each angular bin:

$$X_{ds} = L_s \times \rho_s + L_d \times \rho_d \quad \text{((Equation 3)}$$

where L_s is the path-length of muons through the sedimented materials located at the upstream side of the dam, the ρ_s is the average density of the sediments, L_d is the path-length of muons through the dam and ρ_d is the average density of dam structure. In this study, we determined the quantities X_d and ρ_d for health structural monitoring of the dam. The latter quantity requires the precise measurement of the path-lengths and density of sedimented materials. The average density of sediments was estimated to 1.8 g cm^{-3} via sampling of these materials. The digital elevation model of the measurement site was created with a grid size of 1 m × 1 m based on data acquired by laser profiler by the Ministry of Land, Infrastructure, Transport and Tourism in 2019. The relative young age during which the topography did not change significantly and the sufficient spatial resolution of digital elevation model data enabled us to determine the path-lengths of across the dam and sediments in the coordinate system of the detector for each angular bin. The path-lengths across the dam were calculated using the geometric data of the dam. Figures 6A and 6B show the path-lengths calculated for the dam and for the dam and sediment which ranged up to 4 m and 20 m, respectively. In Figure 6C, the expected density-length is shown with the density values of 2.3 g cm^{-3} and 1.8 g cm^{-3} for the dam and sediments, respectively.

The X_{ds} density-lengths were reconstructed via comparing the measured fluxes (Figure 5B) to modeled fluxes (F_{mod}). The measured flux errors were added to the fluxes to determine the lower density-length errors and were subtracted from the fluxes to calculate the upper density-length errors via the same procedure. The modeled fluxes were determined by integrating the zenith-angle dependent muon momentum spectra from minimum energies that required for muons to penetrate across the sediments and the dam: $F_{mod} = \int_{pmin} f(p,\theta)\, dE$. Here, we applied a parametrization of Ecomug simulation package[71] that is based on the data collected by the ADAMO spectrometer[72]:$f(p,\theta) = [1, 600(p/p_0 + 2.68)^{-3.175}(p/p_0)^{0.279}] \times \cos(\theta)^{n(p)}$, $n(p) = \max[0.1, 2.856–0.655\log(p/p_0)]$ for $p > 0.04$ GeV p_0 equals to 1 GeV. The altitude dependence of muon spectra were taken account via the following formula[73]: $F(H) = F(0)\exp(-H/L(p))$, where $L(p) = 4900 + 750p$. We have to note

that the choice of muon flux model strongly influences the modeled flux (see, e.g., ref. [74]) due to the sparse experimental data below a few tens of GeV. To overcome on this limitation, a rotatable muon spectrometer, called NEWCUT, is under development.[75]

The p_{min} minimum momentums were determined using GEANT4 simulation framework.[76] 5000 monoenergetic muons were generated in each simulation run. The energy was set from 0.1 GeV to 15 GeV. The muons were injected into shielding concrete. The shielding concrete was built up from Oxygen, Silicon, Calcium, Iron, Aluminum and Sodium with the composition ratios of 52%, 32.5%, 6%, 4%, 4% and 1.5%, respectively. The average density of the shielding concrete was set to $\rho = 2.3$ g cm^{-3}. All relevant electromagnetic processes were implemented to accurately simulate the passage of muons in the shielding concrete. The histograms of the range of muons were determined by event-by-event analysis of the simulated data. Figure 7 shows examples of muon range distributions for selected injection energies. The average range values and their sigma values were determined for each histogram. Figure 8 shows the minimum energy versus range for a density-lengths which are comparable with the density-lengths measured across the dam. A second degree polynomial function was fitted on these data to extract the minimum energies for each angular bins: $E(X) = a+bX + cX,^2$ where $a = -0.059 \pm 0.014$, $b = (1888 \pm 1)\times10^{-5}$, $c = (30.3 \pm 1.4)\times10^{-9}$. It is worth noting that we chose a material with density and composition that are close to the inspected dam to derive the relation between the muons' energies and ranges, but other choices are also appropriate because chemical composition result in negligible systematics error at this size scale.[77]

QUANTIFICATION AND STATISTICAL ANALYSIS

There is no statistical analysis in this paper.

ADDITIONAL RESOURCES

We have no relevant resources.